Available online at www.sciencedirect.com
SCIENCE DIRECT®
Continental Shelf Research 25 (2005) 157–183
CONTINENTAL SHELF RESEARCH
www.elsevier.com/locate/csr

Seasonal circulation fields in the northern Gulf of Mexico calculated by assimilating current meter, shipboard ADCP, and drifter data simultaneously with the shallow water equations

S.R. Smith*, G.A. Jacobs

Naval Research Laboratory, Code 7320, Bldg 1009, Stennis Space Center, MS 39529, USA

Received 4 February 2004; received in revised form 16 July 2004; accepted 9 September 2004
Available online 25 November 2004

Abstract

Velocity measurements from current meter moorings, shipboard acoustic Doppler current profilers (ADCPs), and satellite-tracked drifters are used to estimate the seasonally averaged barotropic circulation throughout the continental shelf in the northern Gulf of Mexico in two regions: the Northeast Gulf of Mexico (NEGOM) shelf and the Louisiana–Texas (LATEX) shelf. A variational assimilation approach (weighted least squares) is used to combine the data simultaneously with a system of dynamical equations (time-independent shallow water equations), where the weights are based on the expected errors in the dynamical equations and measurements. Smoothing and boundary constraints are also included in this system to impose a spatial decorrelation scale and to restrict the component of flow that is perpendicular to the coastline, respectively. Seasonal solutions are therefore best fits to the weighted measurements, dynamics, and constraints, and thus do not fit any component exactly. Analysis of the solution deviations to the dynamical equations reveal where and during which seasons the dynamics and data are in disagreement. The largest deviations from the proposed dynamics occur at the head of the DeSoto Canyon on the NEGOM shelf and at the southwest corner of the LATEX shelf. Therefore, in these areas, there are processes occurring that are not described by the simplified barotropic dynamics. At the head of the DeSoto Canyon, the large source of error is believed to be due to deep-ocean water penetrating across the shelfbreak, whereas the process that occurs at the southwest corner of the LATEX shelf is proposed to be a result of a convergence zone caused by loop current eddies. Error analysis reveals that current meter data are more capable of constraining the solution than the other two data types due to its ability to more accurately observe barotropic currents. Separate experiments are conducted using the shipboard ADCP and drifter data sets individually to determine the relative observation capability. These experiments reveal that both data types provide reasonable estimations of seasonal flow fields. Results on the LATEX shelf suggest that shipboard ADCP data is more capable of observing the seasonal barotropic flow than drifter data. Whereas, on the

*Corresponding author. Fax: +1 228 688 4759.
E-mail address: smithsc@nrlssc.navy.mil (S.R. Smith).

0278-4343/$ - see front matter Published by Elsevier Ltd.
doi:10.1016/j.csr.2004.09.010

NEGOM shelf results imply that drifter data are more capable. This result, however, may be skewed due to the shipboard ADCP and drifter data sets being collected during different years.
Published by Elsevier Ltd.

Keywords: Barotropic motion; Continental shelves; Least-squares method; Eulerian current measurement; Lagrangian current measurement; Gulf of Mexico

1. Introduction

The study area on the northern Gulf of Mexico continental shelf extends from the shore to the 200 m isobath and is split into two regions separated by the Mississippi River Delta. The northwestern region consists of the Louisiana–Texas (LATEX) shelf and the Northeast Gulf of Mexico (NEGOM) includes the Mississippi–Alabama shelf (Fig. 1). Seasonal circulation fields are calculated and analyzed individually for these two regions.

Prior work (Cochrane and Kelly, 1986; Vastano et al., 1995; Cho et al., 1998) suggests that the general circulation on the LATEX shelf during September–May is dominated by a cyclonic gyre, consisting of a strong westward coastal current and a relatively weak eastward current along the shelfbreak. This gyre disappears during June–August and the flow is directed toward the Mississippi delta over the entire shelf. As is typically the case in coastal regions, the flow on the LATEX shelf is primarily wind driven, and the correlation between the along-shore component of current and the along-shore component of wind stress increases closer to the shore (Chen et al., 1996). In addition to wind stress, river buoyancy from the Mississippi and Atchafalaya Rivers and mesoscale eddies can also have a significant impact on the flow field (Oey, 1995; Li et al., 1997). For example, Oey (1995) estimates that a peak southwestward transport of 0.21–0.25 Sv ($1\,\mathrm{Sv} = 10^6\,\mathrm{m}^3/\mathrm{S}$) occurs close to the shore in autumn, of which 0.1 Sv is due to wind, 0.07 Sv is due to river buoyancy, and 0.04–0.08 Sv is due to eddies. Along the shelfbreak, however, it is believed by Oey (1995), Jochens, (1997), Li et al. (1997), and Cho et al. (1998) that the circulation is dominated by anticyclonic loop current eddies (LCEs) along with associated cyclonic eddies and only seasonally modulated by the wind-induced flow.

Prior work in the NEGOM region (Hamilton et al., 2000; He and Weisberg, 2002; Hsueh and Golubev, 2002; Wang et al., 2003) concludes that the overall general flow is predominantly eastward and the circulation varies significantly on both the seasonal and interannual time scales. This eastward flow is believed by Golubev and Hsueh (2002) to be an extension of the predominantly southward flow along the West Florida shelf caused by a drop in dynamic pressure when the loop current (LC) has minimum northward protrusion. When the LC reaches its maximum northward penetration, the pressure drop is much weaker leading to a much weaker southward current. The primary source of variability on the NEGOM shelf is proposed by Golubev and Hsueh (2002) and Weisberg and He (2003) to be a combination of deep-ocean processes and local forcing. Wang et al. (2003) suggest that the DeSoto Canyon region is typically not directly influenced by the LC or LCEs except on rare occasions when the LC or an LCE extrude sufficiently northward. Weisberg and He (2003) explain that the LC helps elevate material isopleths along the shelf slope allowing local forcing to upwell material across the shelfbreak. Once on the shelf, local forcing typically plays the dominant role in distributing material. On rare occasions, however, deep-ocean effects can dominate the distribution of material on the shelf, as was the case during the spring–fall seasons of 1998 (Weisberg and He, 2003; He and Weisberg, 2003).

The continental shelf in the northern Gulf of Mexico has been the site for many research studies. These studies deployed many different types of instruments in the attempt to estimate the general circulation and understand various physical processes. Some of the instruments used to measure water properties include current meter moorings, ADCP moorings, shipboard ADCPs,

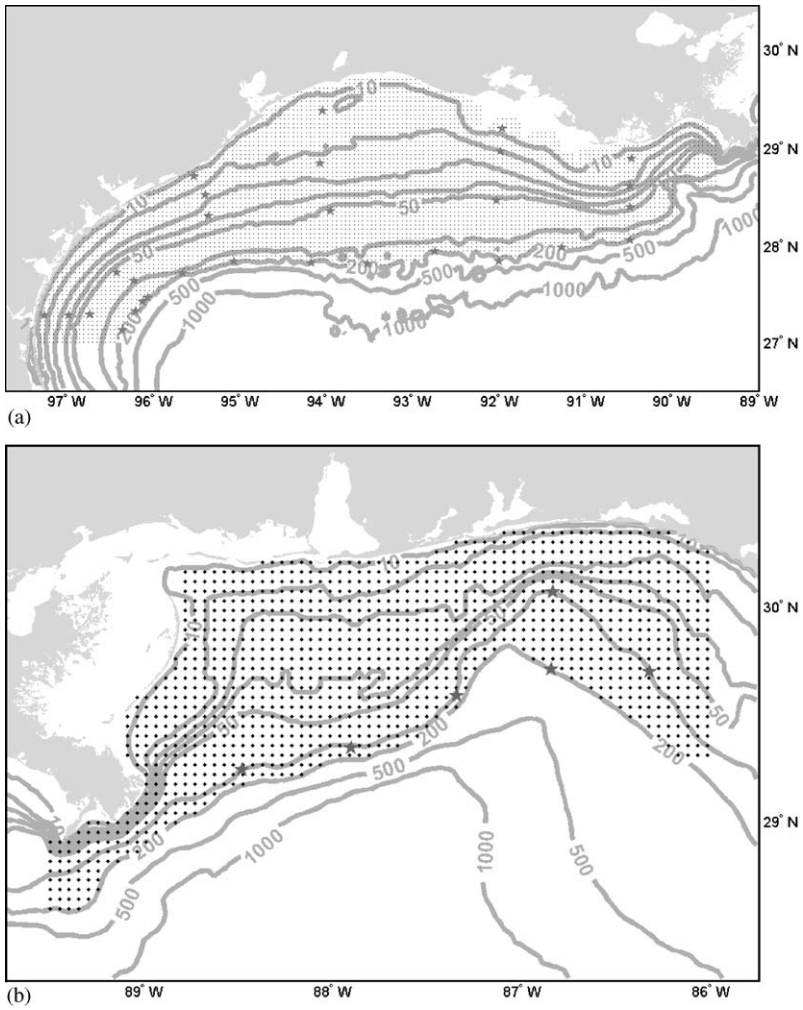

Fig. 1. Areas covered within this study are the (a) LATEX and (b) NEGOM shelves. The gray contours are isobaths (m), the dots are grid points at which solutions are computed (10 km resolution), and the gray stars show the locations of the current meter moorings from the (a) "LATEX A Study" and the (b) "DeSoto Canyon Eddy Intrusion Study".

drifters, satellite altimetry, buoys, AXBTs, XBTs, CTDs, and satellite infrared imagery. Typically, only one type of data is examined and used in isolation of others. For example, Cochrane and Kelly (1986) use hydrographic data and Cho et al. (1998) use current meter measurements to estimate the general circulation on the LATEX shelf. Whereas, the general circulation on the NEGOM shelf is estimated by Schroeder et al. (1987) and Golubev and Hsueh (2002) using the movement of detached buoys and satellite-tracked drifters, respectively. In this paper, three different types of velocity data are used simultaneously in the estimation of the overall mean seasonal circulation fields on the LATEX and NEGOM shelves.

In order to bring as much information to the solution simultaneously as possible, observations are merged with a system of dynamics using a variational assimilation approach (inverse theory). Assimilation of data into models is typically conducted by integrating a forward model to the observation time, computing the difference between the model and observations, analyzing a correction to the model, and continuing to the next

observation time (Talagrand, 1997; Robinson et al., 1998). These methods may be generalized beginning with a variational minimization of a cost function (Le Dimet and Talagrand, 1986). The methodology employed here is the same. However, the model of this study is composed of equations that are time invariant; thus, dramatically reducing the state space for the problem at hand. This saving allows the solution here to be approached through a direct minimization of the cost function. Within this paper, assimilation of data refers to the process of minimizing the cost function containing both the dynamical equations and data.

Each observation type is capable of making a unique and valuable contribution to the solution, as do the dynamical equations. Thus, it is important to bring these different pieces of knowledge together in a uniform manner. A difficult part of this problem is determining the level of contribution (weight) each component makes to the solution. This information is embedded within the expected errors of each measurement type and dynamical equation. While certain methods are available to specify particular error contributions, many others must be made rather subjectively. However, it is possible to test the solution sensitivity to variations in these judgments to insure the solution does not significantly change over a wide range of error estimates.

A discussion of the domains in which seasonally averaged flow fields are estimated is provided in Section 2. The data sets that are used in this estimation are described in Section 3 and include SCULP drifter data and current meter mooring and shipboard ADCP measurements from the "LATEX A Study", the "DeSoto Canyon Eddy Intrusion Study", and the "Northeastern Gulf of Mexico Physical Oceanography Program: Chemical Oceanography and Hydrography Study". A weighted least-squares technique is used in this study to combine these different data sets with a system of specified dynamics, including momentum, continuity, and boundary and smoothing constraints. These dynamics are appropriate for time-independent barotropic shallow water flow and are discussed in Section 4.

A preconditioned conjugate gradient inverse method is used to determine the vertically integrated and seasonally averaged velocity fields that best satisfy the weighted data and dynamics (vertically integrated velocity is hereinafter referred as transport). A discussion of this method, including the determination of the expected errors in the data and dynamics, is given in Section 5. In Section 6, a discussion of the results and the errors in the dynamics and measurements associated with these results is provided. Even though each region contains relatively dense observations, the solution obtained by only smoothing the observations is significantly different from that obtained by including the dynamics. Thus, it is important to simultaneously consider physical properties along with the observations when constructing ocean environment estimates.

Since the solution is a least-squares fit to the observations and proposed dynamics, it satisfies neither exactly. Examination of the solution mismatch to the observations indicates which observation type best estimates the general circulation, and the errors to the dynamics reveal where and during which seasons the solution deviates significantly from the prescribed equations of motion. Generally, the largest deviations from the proposed dynamics occur along the shelfbreak. This is an area in which baroclinic processes are expected to occur, thus causing the simple proposed barotropic dynamics to fail. Finally, some concluding remarks are given in Section 7.

2. Domain

Solutions of seasonally averaged transport and sea surface height (SSH) are computed on a discretized grid (Fig. 1). The solution domains consist of 157×62 and 69×43 grid points on the LATEX and NEGOM shelves, respectively, with a grid spacing of $\Delta x = \Delta y = 10\,\mathrm{km}$. The equations of motion are discretized using an Arakawa A grid (Mesinger and Arakawa, 1976). This grid spacing is sufficient to provide at least 2–3 grid points for typical features. Li et al. (1996) use hydrographic data from the LATEX A Study to conclude that typical spatial scales in the cross-shelf direction are

on the order of 15–20 and 35 km in the along-shelf direction. The numerical grid representing the dynamics excludes points with water depths less than 5 m or greater than 200 m as well as grid points that are not a part of at least four connecting water grid points in both the meridional and zonal directions. This is because at least four consecutive grid points are required in order to perform a second-order accurate finite difference operation at a boundary point. The application of this masking to the domains results in 4472 and 1224 grid point locations on the LATEX and NEGOM shelves, respectively.

3. Data sets

Three data sets are used in this study with all measurements being converted to vertically integrated transports. Certain data sets are more capable of providing vertically integrated transports than others, and the uncertainty associated with this is included in the weighting used in the least-squares process (discussed in Section 5). The first data set is comprised of seasonally averaged transports computed from moored current meter data. The second and third sets of data include transports computed from shipboard ADCP and drifter data, respectively. Fig. 2 shows the temporal distribution of measurements collected from these data types on both the LATEX and NEGOM shelves. The dates encompassing each season in Fig. 2, and hence throughout this paper, are based on the average equinoxes: March 21–June 20 (spring), June 21–September 22 (summer), September 23–December 21 (autumn), and December 22–March 20 (winter). Overall, a tremendous number of individual measurements are assimilated. With all seasons combined, a total of 39,164 and 15,324 measurements are assimilated on the LATEX and NEGOM shelves, respectively. The description and processing of each observation type is considered in this section.

3.1. Current meter moorings

The current meter measurements used on the LATEX shelf are from 29 of the 33 moorings deployed from April of 1992 to December of 1994 (Fig. 2a) as part of the "Texas–Louisiana Shelf Circulation and Transport Processes Study" (LATEX A Study) sponsored by the Minerals Management Service (DiMarco et al., 1997). The locations of these moorings are scattered across the LATEX shelf (Fig. 1a). Four of the moorings were in depths greater than 200 m, which is beyond the solution domain. Moorings in shallow water consisted of one current meter whereas moorings closer to the shelfbreak consisted of up to 3. The data from these current meters were filtered using two Lanczos filters; first a 3 h low-pass filter was used to remove signal noise then a 40 h low-pass filter was used to remove tidal and inertial motions (DiMarco et al., 1997).

The current meter measurements used on the NEGOM shelf are from six of the 13 bottom mounted ADCP moorings (hereafter called current meters) deployed from March 1997 to April 1999 (Fig. 2b) by Science Application International Corporation as a part of the "DeSoto Canyon Eddy Intrusion Study" sponsored by the Minerals Management Service (Hamilton et al., 2000). Five current meters are located along the 100 m bathymetry contour and the sixth current meter is located on the 200 m contour. Seven of the NEGOM DeSoto Canyon current meters were deployed at depths greater than 200 m, which is beyond the solution domain. Each of these meters, except the meter on the 200 m contour, contained an upward looking RD Instruments (RDI) Workhorse ADCP positioned at 80–90 m depth and an InterOcean current meter at approximately 6 m above the bottom. The meter on the 200 m contour contained a 150-kHz RDI narrowband ADCP positioned at 180 m depth. All the raw data received were filtered with a 40 h low-pass filter (Hamilton et al., 2000).

3.2. Shipboard acoustic Doppler current profiler

Two 150-kHz narrowband ship-mounted ADCPs, manufactured by RDI, were in operation during nine of the hydrographic surveys conducted as part of the "LATEX A Study". These nine surveys were interspersed throughout the same 32 month time period covered by the moorings

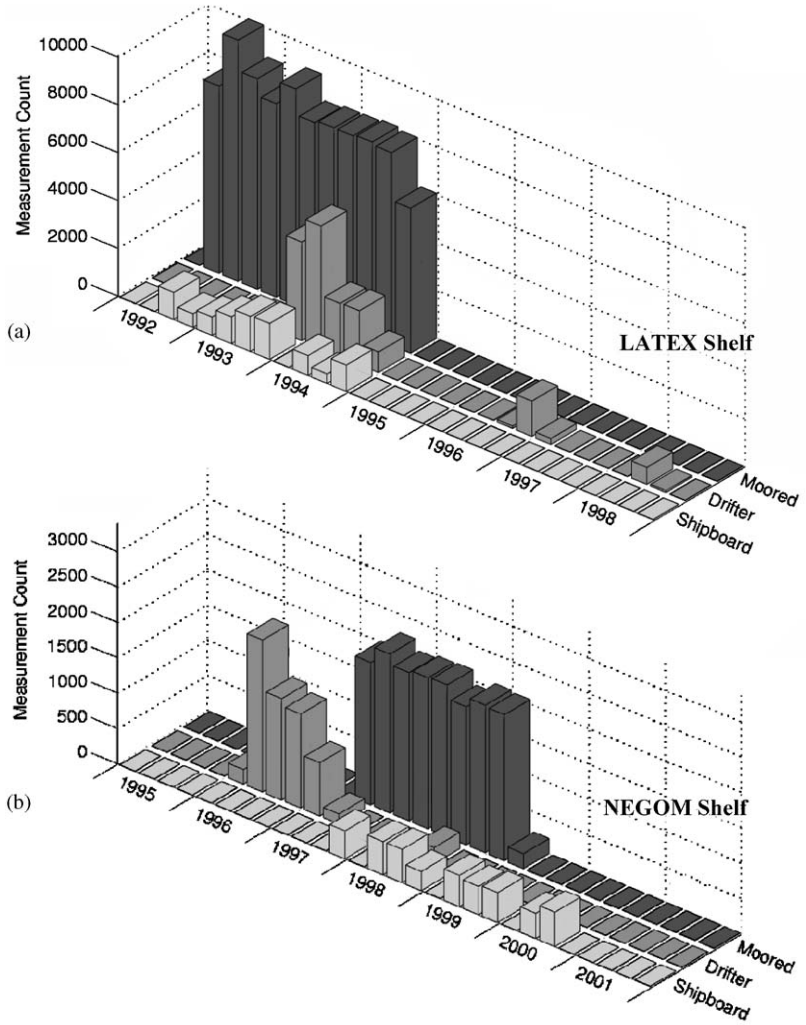

Fig. 2. Temporal distributions of current meter, shipboard ADCP, and drifter velocity measurements collected on the (a) LATEX shelf indicate that the majority of these measurements were collected during the "LATEX A Study". Whereas, on the (b) NEGOM shelf the majority of drifter measurements do not coincide with the sampling of current meter and shipboard ADCP measurements made during the "DeSoto Canyon Eddy Intrusion Study" and the "Northeastern Gulf of Mexico Physical Oceanography Program: Chemical Oceanography and Hydrography Study", respectively. The bins in these histograms denote the number of measurements of each data type collected during each season, where the first bin of each year represents winter. Each of these measurements represents both velocity components and the entire vertical profile of the actual observations made within the solution grid from each instrument at each time increment. Velocity observations were made or inferred in 5 min, 6 h, and 1 day time increments using shipboard ADCPs, current meters, and drifters, respectively.

(Fig. 2a). Each cruise lasted roughly 1–2 weeks and covered various portions of the LATEX shelf. Data from each cruise contained velocity measurements in 4 m depth increments and 5 min intervals (Bender and Kelly, 1996).

On the NEGOM shelf nine hydrographic surveys were performed between autumn of 1997 and summer of 2000 (Fig. 2b) as part of the "Northeastern Gulf of Mexico Physical Oceanography Program: Chemical Oceanography and

Hydrography Study'' sponsored by the Minerals Management Service. An RDI NB 150 ship-mounted ADCP was in use during each of these surveys, which crisscrossed the entire shelf. Similar to the surveys performed on the LATEX shelf, each cruise lasted about 2 weeks and velocity measurements were collected in 4 m depth increments and 5 min intervals (Jochens et al., 2002).

3.3. SCULP drifters

Hundreds of CODE-type Lagrangian drifters were released and tracked via ARGOS throughout the northern Gulf of Mexico as part of the SCULP program (Fig. 2). Once deployed, these drifters were drogued at a depth of 1 m while periodically reporting position via satellite. Based on reported positions and the time between position reports, velocities are computed. Dr. Peter Niiler (pers. comm.) created a comprehensive database of the daily position and average velocity of all drifters.

3.4. Data preparation

All of the measurements that fell within the solution domain are assimilated at the nearest grid point. The measurements of u and v made by each current meter are vertically integrated and seasonally averaged prior to assimilation. Since the current meters have fixed locations, there is not a significant difference in solutions when assimilating the seasonally averaged transports instead of all the individual transports, which are at every 6 h interval. The main difference lies in the weight applied to individual observations versus seasonally averaged observations. Individual observations are not as representative of the seasonally averaged flow and thus contain a greater error than seasonally averaged observations. This simplification greatly reduces the size of the problem without altering the solution. For the shipboard ADCP measurements, each vertical velocity profile measured at a 5 min interval is vertically integrated. For the SCULP drifter data each inferred velocity measurement is multiplied by the total depth to provide transport. Since drifter data consists of only one measurement at the surface, the errors associated with measuring barotropic flow from the SCULP drifters are much larger than those associated with the ADCP measurements (estimation of these errors is discussed in detail in Section 5).

Fig. 2 reveals that on the LATEX shelf the current meter, shipboard ADCP, and the vast majority of drifter data were collected during the same time period. However, on the NEGOM shelf the majority of drifter data was collected in the year prior to the mooring deployments. During each of the LATEX and NEGOM Studies, a majority of the shelf areas are sampled (Figs. 3 and 4). These figures show that there are considerable differences between the three data types within each season. The largest differences appear to be between the shipboard ADCP and drifter measurements on the NEGOM shelf, particularly along the coast. Since the NEGOM drifter measurements occur during different years from the other two data types, it is believed that these differences are mostly due to interannual variations. Difference between data types can also be expected since the measurements in each data type use different measuring devices, are processed differently, and occur at different locations and times. This is one of the main reasons why data from different sources are rarely combined to make flow field estimations.

4. Dynamics

4.1. Equations of motion

The governing physics used to constrain this system are the conservation of mass and momentum. These equations of motion are based on the shallow water equations, which are a simplification of the fundamental Eulerian equations of motion. The assumptions underlying these equations are that the flow is barotropic and hydrostatic. Additional simplifications include the Boussinesq, and linear approximations. These simplified equations of motion are Reynolds averaged over seasonal time scales and the time rate of change of all variables are neglected so that the equations represent the dynamics of the seasonally averaged

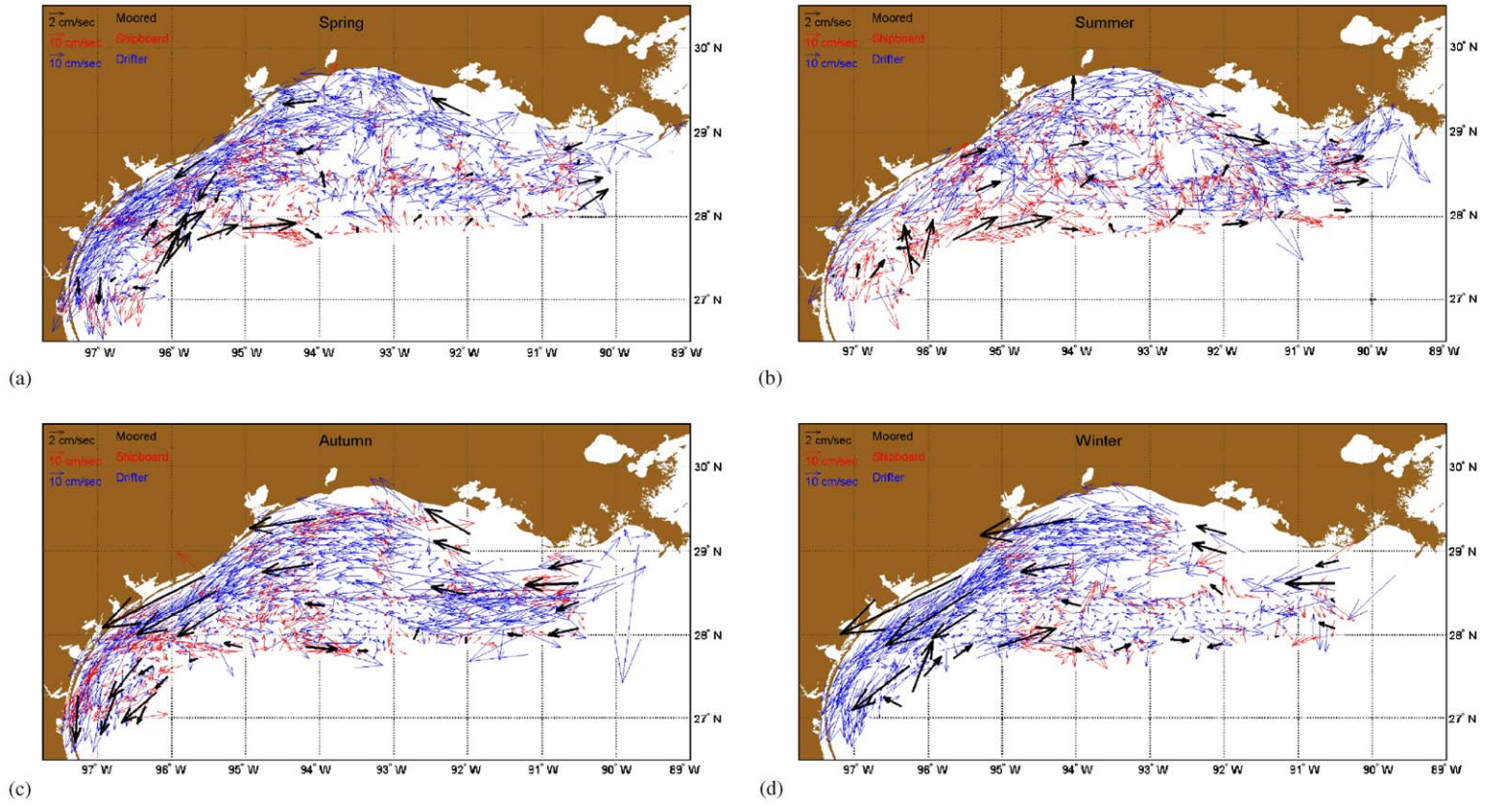

Fig. 3. Depth averaged current meter (black vectors), shipboard ADCP (red vectors), and drifter (blue vectors) velocity measurements that are assimilated on the LATEX shelf show significantly different flow fields between data types. For this figure, the measurements that were collected during (a) spring, (b) summer, (c) autumn, and (d) winter are spatially weighted to their nearest solution grid points and averaged. Note that the scale for the current meter measurements is five times less than the scales for the shipboard ADCP and drifter measurements. The current meter measurements are smaller since they are seasonally averaged (thus reducing the effects of instantaneous fluctuations) and the shipboard ADCP and drifter measurements are not.

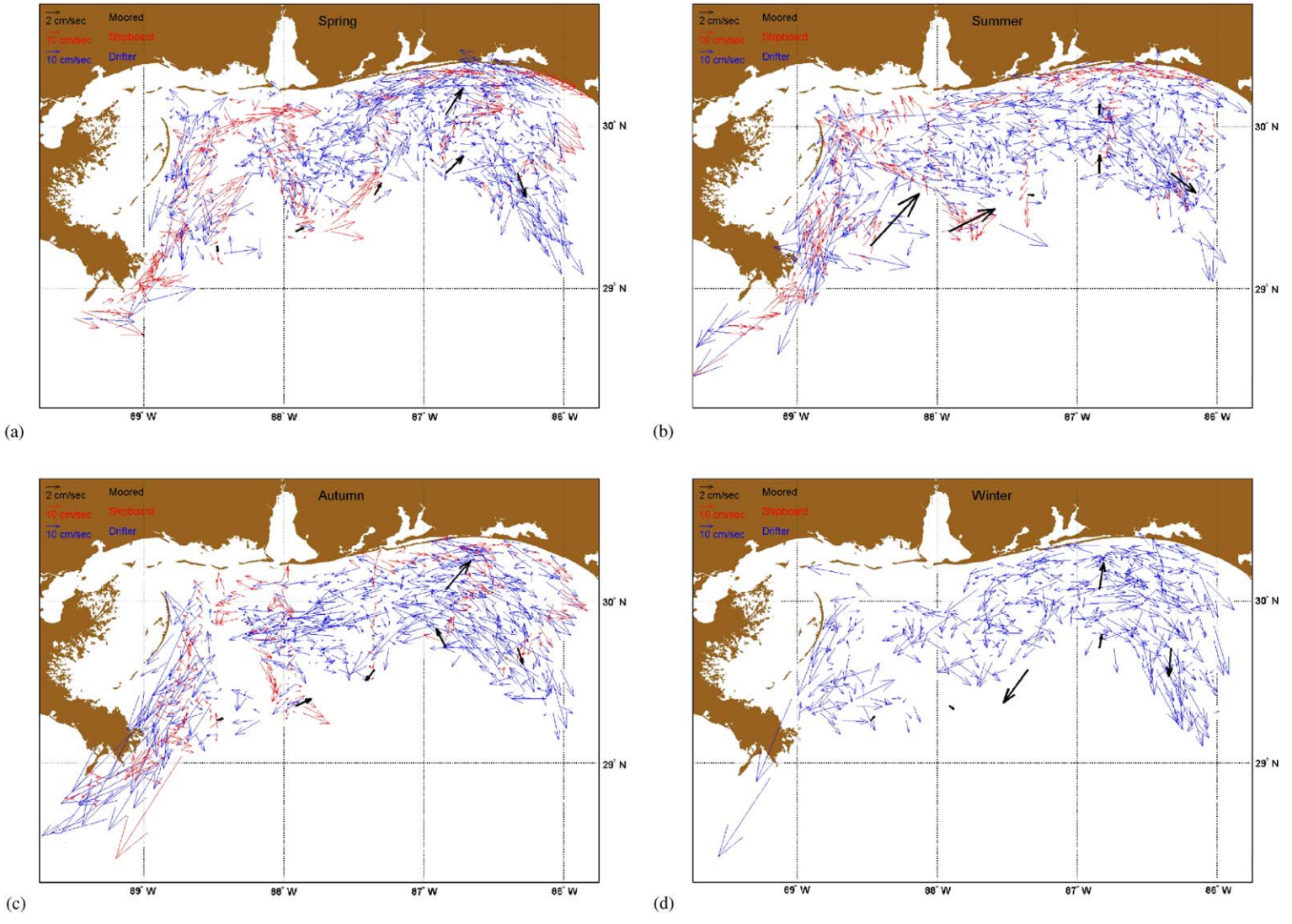

Fig. 4. This figure is the same as Fig. 3 except that it is for the NEGOM shelf. Also, there are no shipboard ADCP measurements for (d) winter because no research cruises during the "Northeastern Gulf of Mexico Physical Oceanography Program: Chemical Oceanography and Hydrography Study" occurred during this season (see Fig. 2b).

flow fields:

$$\frac{\partial U}{\partial x}+\frac{\partial V}{\partial y}=0, \tag{1}$$

$$fV-gH\frac{\partial\bar{\eta}}{\partial x}+K_{\mathrm{H}}\left(2\frac{\partial^2 U}{\partial x^2}+\frac{\partial^2 U}{\partial y^2}+\frac{\partial^2 V}{\partial x\partial y}\right)-C_{\mathrm{D}}\left|\vec{u}_{\mathrm{B}}\right|\frac{U}{H}=-\frac{\tau_x}{\rho_0}, \tag{2}$$

$$-fU-gH\frac{\partial\bar{\eta}}{\partial y}+K_{\mathrm{H}}\left(\frac{\partial^2 V}{\partial x^2}+2\frac{\partial^2 V}{\partial y^2}+\frac{\partial^2 U}{\partial x\partial y}\right)-C_{\mathrm{D}}\left|\vec{u}_{\mathrm{B}}\right|\frac{V}{H}=-\frac{\tau_y}{\rho_0}, \tag{3}$$

where U, V, and $\bar{\eta}$ are the two components of transport and SSH, respectively, that are solved at all grid points.

The Coriolis parameter (f) in the above momentum equations varies with latitude. The bathymetry (H) is interpolated from a 2-min resolution Naval Research Laboratory product called NRL DBDB2. DBDB2 is based on DBDB5 and includes all the DBDBV high-resolution data along with additional very high-resolution localized bathymetry data sets. The value used for the horizontal eddy viscosity coefficient, $K_{\mathrm{H}}=1000.0\,\mathrm{m^2/s}$, is a high estimate based on output from the Navy Coastal Ocean Model during an energetic event on the NEGOM shelf. Even with a large value of K_{H}, the smoothing effect that diffusion has on the solution is minor compared to the influence of the smoothing constraint (discussed in Section 4.2). The bottom drag coefficient $C_{\mathrm{D}}=0.002$ is a commonly used value for the ocean floor (Csanady, 1984). The average magnitude of bottom velocity ($|\vec{u}_{\mathrm{B}}|$) is computed for each season and region individually by seasonally averaging the magnitude of all current meter data within the bottom 10 m of the water column. The spatially averaged density (ρ_0) is estimated for each season and region individually using the modular ocean data assimilation system (MODAS), which is one of the present US Navy standard tools for production of static, bimonthly, three-dimensional grids of temperature and salinity using all available historical observations (Fox et al., 2002). The seasonally averaged wind stress components (τ_x and τ_y) are calculated from five years (January 1997–December 2001) of Navy Global Ocean and Atmospheric Prediction System (NOGAPS) output (Hogan and Rosmond, 1991). A bicubic spline fit is used to interpolate the NOGAPS wind stress fields, which has a resolution of 1° spatially and 6 h temporally, to the solution grid points on the LATEX and NEGOM shelves.

4.2. Physical constraints

Coastal boundary and smoothing constraints are also included in the set of dynamics. The coastal boundary constraint forces the cross-shore component of flow to be zero at the solution grid points that border land:

$$U\hat{n}_x+V\hat{n}_y=0, \tag{4}$$

where $\hat{n}_x$ and $\hat{n}_y$ are the normal components in the meridional and zonal directions, respectively, of the vector perpendicular to the coastline and are calculated by using the normalized gradients of bathymetry:

$$\hat{n}_x=\frac{\partial H/\partial x}{\sqrt{(\partial H/\partial x)^2+(\partial H/\partial y)^2}}$$

and

$$\hat{n}_y=\frac{\partial H/\partial y}{\sqrt{(\partial H/\partial x)^2+(\partial H/\partial y)^2}}.$$

Solution grid points along the shelfbreak, however, are considered open and have no constraint.

The second constraint is required to remove features that are not resolved on the discretized solution grid or by the measurements. The smoothing constraint is applied by setting the Laplacian plus a second-order cross derivative of each of the solution variables to zero:

$$\frac{\partial^2 U}{\partial x^2}+\frac{\partial^2 U}{\partial y^2}+\frac{\partial^2 U}{\partial x\partial y}=0, \tag{5}$$

$$\frac{\partial^2 V}{\partial x^2}+\frac{\partial^2 V}{\partial y^2}+\frac{\partial^2 V}{\partial x\partial y}=0, \tag{6}$$

$$\frac{\partial^2\bar{\eta}}{\partial x^2}+\frac{\partial^2\bar{\eta}}{\partial y^2}+\frac{\partial^2\bar{\eta}}{\partial x\partial y}=0. \quad (7)$$

Without this constraint, the solution could be filled with many small-scale features not resolved by the measurement array and yet still satisfy the dynamical equations.

5. Method

The solution is defined as the set of seasonally averaged transports and SSH at the solution grid points that best fit the weighted discretized equations of motion, physical constraints, and data simultaneously. The discretization of the equations of motion (Eqs. (1)–(3)), and smoothing constraints (Eqs. (5)–(7)) are applied at each solution grid point for each season. Derivatives in these equations are discretized using second-order accurate finite differencing. The boundary constraint (Eq. (4)) is applied only at the grid points that border land. The data that fall within either region are applied at the grid points closest to the actual locations of the measurements. For each region, all equations representing the data and dynamics at their appropriate solution grid points are solved simultaneously for all seasons, resulting in approximately 130,000 equations in the LATEX problem and 38,000 equations in the NEGOM problem. Since there are 53,664 unknowns in the LATEX problem and 14,688 unknowns in the NEGOM problem, these problems are over-determined.

5.1. Weighted least-squares and conjugant gradient methods

The solution to this over-determined problem is constructed using a weighted least-squares approach. For each region the system of equations can be written in matrix form as

$$\mathbf{A}\vec{\mathbf{x}}=\vec{\mathbf{b}}. \quad (8)$$

The coefficient matrix ($\mathbf{A}$) contains the discretization of the left-hand side of the continuity, momentum, boundary constraint, smoothing, and measurement equations at all applicable solution grid points. The state vector ($\vec{\mathbf{x}}$) contains the unknown variables for which a solution is sought (U, V, and $\bar{\eta}$ at all grid points) and the forcing vector ($\vec{\mathbf{b}}$) consists of the right-hand side of the continuity, momentum, boundary constraint, smoothing, and measurement equations. For example, one row of the $\mathbf{A}$ matrix that contains the continuity equation at an interior grid point (i,j) multiplying the state vector and set equal to its corresponding element of $\vec{\mathbf{b}}$ is

$$\left[\cdots\frac{1}{\mathrm{d}x}\cdots\frac{-1}{\mathrm{d}x}\cdots\frac{1}{\mathrm{d}y}\cdots\frac{-1}{\mathrm{d}y}\cdots\right]\times\left[\ldots U_{i+1,j}\ldots U_{i-1,j}\ldots V_{i,j+1}\ldots V_{i,j-1}\ldots\right]^{\mathrm{T}}=0. \quad (9)$$

The dots in the first term represent zero elements within $\mathbf{A}$ and the dots in the second term represent state variables within $\vec{\mathbf{x}}$ that are multiplied by these zeros. Similarly, the two rows that contain the components of a velocity measurement at the same grid point are

$$\begin{bmatrix}\ldots 1\ldots\\ \ldots 1\ldots\end{bmatrix}\left[\ldots U_{i,j}\ldots V_{i,j}\ldots\right]^{\mathrm{T}}=\begin{bmatrix}U_m\\ V_m\end{bmatrix}, \quad (10)$$

where the right-hand side contains the values of this measurement.

The state vector ($\vec{\mathbf{x}}$) that best satisfies Eq. (8) is a solution to

$$\mathbf{A}^{\mathrm{T}}\mathbf{W}\mathbf{A}\vec{\mathbf{x}}=\mathbf{A}^{\mathrm{T}}\mathbf{W}\vec{\mathbf{b}} \quad (11)$$

which is the weighted least-squares formulation. The weighting matrix ($\mathbf{W}$) is the inverse of the error covariance matrix, which is comprised of the expected errors in each of the continuity, momentum, boundary, smoothing, and measurement equations. The matrix $\mathbf{A}^{\mathrm{T}}\mathbf{W}\mathbf{A}$ in Eq. (11) is square and has full rank; therefore, it can be inverted allowing a solution to be obtained. Instead of inverting, an iterative preconditioned conjugate gradient technique is used to solve for the state that minimizes the total error to the weighted dynamics and measurements:

$$\text{Total error}=(\mathbf{A}\vec{\mathbf{x}}-\vec{\mathrm{b}})^{\mathrm{T}}\mathbf{W}(\mathbf{A}\vec{\mathbf{x}}-\vec{\mathbf{b}}). \quad (12)$$

The conjugate gradient solver uses a 1-step Jacobi preconditioner (Barrett et al., 1994) and is applied

iteratively until the total cost difference between successive iterations relative to the initial cost is less than 10^{-6}. While intensive indexing is needed to represent the discretized form of the dynamical equations, constraints, and observations within $\mathbf{A}$ and the state variables within $\vec{\mathbf{x}}$, the conceptual framework does not deviate from the basic theory of least squares (Eq. (11)). While conceptually simple, the actual application to the problem at hand is most difficult with regards to determining the weights and understanding the impact of these weights on the solution.

5.2. Weighting matrix

One of the most important aspects of any inversion or statistical estimation scheme is the covariance errors describing the accuracy of the dynamical equations and measurements. These errors include the neglected terms in the dynamic equations, parameterization of dynamical processes, errors in the forcing of the dynamical equations, sensor errors in measurements, and representativeness errors. The weighting matrix that is used in this solution process is a diagonal matrix with elements consisting of the reciprocal of the expected variance $(1/\langle \mathrm{er}^2 \rangle)$ in continuity, momentum, boundary, smoothing, and the three different data types. By neglecting the cross-covariances of the expected errors, the problem is better conditioned allowing quicker convergence of the conjugate gradient. For simplicity, it is also assumed that the expected variance in each of the equations of motion, constraints, and measurements are the same at all grid points and during all seasons (spatially and temporally homogeneous).

In order to maintain the correct proportion of weights within the total cost function so that they are independent of the number of grid points or measurements, the weight for each component is divided by its number (n) of discretized equations for each season within the coefficient matrix. For example, the weight applied to each continuity equation is

$$\mathbf{W}_{\mathrm{Continuity}} = \frac{1}{n_{\mathrm{Continuity}} \langle \mathrm{er}^2_{\mathrm{Continuity}} \rangle}. \tag{13}$$

For continuity, momentum, and smoothing n is equal to the number of grid points; for coastal boundary constraints n is equal to the number of grid points that border land; and for data n is equal to the number of measurements that are assimilated for each season. This definition of the weights assures that each contribution to the cost function can be modeled as a Chi-squared variable with an expected value of one and is of comparable magnitude. For example, if the contributions to the cost function are not divided by n, a doubling of resolution would place a factor 4 greater weight on the dynamical equations.

Optimally, the expected error in each of these dynamical equations and data types should include all error resulting from neglected terms, approximations, and discretization. However, it is well beyond the scope of this study to account for all of these error sources. Therefore, expected errors are approximated by only considering the hypothesized primary sources of error in each dynamical equation and data type for each region. The solution sensitivity to variations of each weight is checked to insure that these rough estimates of error will not severely alter the conclusions.

The primary source of error in the continuity equation (Eq. (1)) is believed to be the neglecting of time rate of change of SSH $(\partial\bar{\eta}/\partial t)$. This neglected value is estimated by seasonally averaging 10 years of TOPEX altimeter data at each of its data points that are within either region. The magnitudes of the differences in SSH between consecutive seasons at all data points are then averaged. These errors (along with the errors associated with the other sets of dynamics and data) are given in Table 1. Note that the large range in values of expected errors in Table 1 is due to the different equations and measurements having different physical representation and thus different units.

In the derivation of the momentum equations (Eqs. (2) and (3)), many assumptions are made. Several terms are neglected, and depending on the location and time of year the largest of these tentative sources of error might differ significantly. This makes estimating the primary source of error an extremely difficult task to perform. There is not

Table 1
Estimated expected RMS errors for the different components of dynamics and data that are needed to construct the weighing matrices for the LATEX and NEGOM shelves

	LATEX			NEGOM		
	n		Expected error	n		Expected error
Continuity (m/s)	4472		6.24×10^{-9}	1224		5.91×10^{-9}
Momentum (m^2/s^2)	4472		2.96×10^{-5}	1224		1.96×10^{-5}
Smoothing of U and V (1/s)	4472		7.20×10^{-8}	1224		6.98×10^{-8}
Smoothing of SSH (1/m)	4472		3.16×10^{-10}	1224		3.03×10^{-10}
Boundary constraint (m^2/s)	260		7.20×10^{-2}	108		6.98×10^{-2}
Current meter (m^2/s)	29	29	2.20	6	6	3.16
	28	27		6	6	
Shipboard ADCP (m^2/s)	1895	2930	9.26	1209	1322	8.25
	3083	763		1081	0	
Drifter (m^2/s)	1850	1639	13.70	1457	1096	9.08
	3930	3379		852	621	

Note: n is the number of discretized equations of each dynamical and data component for each season within the coefficient matrix. These values are required in Eq. (13) so that each weighted component has an equal contribution within the cost function. The value of n for measurements is different for each season: upper-left, upper-right, lower-left, and lower-right values correspond to spring, summer, autumn, and winter, respectively.

a procedure for estimating many of the neglected terms. This requires estimates based on magnitudes of known terms and the assumption that neglected terms can be of comparable magnitude. Certainly, neglected terms should be smaller or else our a priori choice of dynamical equations would be exceptionally misleading. However, this provides an upper bound on the dynamical errors. We assume that errors are no larger than the terms that have been retained in the momentum equations. Therefore, the upper bound of momentum error is approximated by averaging the magnitude of the wind stress on the LATEX and NEGOM shelves using all 5 years of NOGAPS data.

The purpose of the smoothing constraints is to filter out features not resolved by the observing system or the numerical grid. Therefore, the expected error in smoothing is set equal to the reciprocal of the square of the discretization ($1/\Delta x^2$ or $1/\Delta y^2$). Since smoothing is applied to both transport and SSH, the expected errors are normalized by multiplying them by the average magnitude of the transport measurements and TOPEX data, respectively. The primary error in the coastal boundary constraint is believed to be a result of not including river runoff and is estimated to be 10% of the mean magnitude of the transport measurements.

The errors associated with the measurements can be more rigorously computed using standard methods. Measurement errors can be broken down into two sources. The first is accuracy in the instrument (sensor error) and the second is the lack of representation of the observation (representativeness error). The primary source of error in current meter measurements is a result of using individual measurements to represent seasonally averaged velocities (a type of representativeness error). This error is estimated by first determining the sinusoid function with a one cycle per year frequency ($\mathbf{U}^{\mathrm{H}}$) that best fits the time series of vertically integrated velocities from each current meter mooring location ($\mathbf{U}$). The root mean square (RMS) of the differences between the vertically integrated current meter measurements and the one cycle per year fit is

$$\mathrm{RMS}(\mathbf{U}-\mathbf{U}^{\mathrm{H}}) = \begin{cases} 9.26\,\mathrm{m}^2/\mathrm{s}, & \text{LATEX}, \\ 8.25\,\mathrm{m}^2/\mathrm{s}, & \text{NEGOM}, \end{cases} \tag{14}$$

where $\mathbf{U}$ and $\mathbf{U}^{\mathrm{H}}$ include both components of transport.

Since the current meter measurements are seasonally averaged prior to assimilation, these errors are divided by the equivalent degrees of freedom. The equivalent degrees of freedom are estimated by $\sqrt{T/\tau}$, where T is the time period spanning the seasonally averaged data and τ is the time scale of events (13.77 and 26.73 days for the LATEX and NEGOM shelves, respectively). The event time scales are calculated for each region by averaging the decorrelation time (time of the first zero-crossing of the lagged auto-correlation of $\mathbf{U}-\mathbf{U}^{\mathrm{H}}$) of each velocity component from each current meter. Seasonal averaging is straight forward for the current meter data, since they are at constant positions. However, if individual current meter measurements were used, the expected errors would just be the RMS values in Eq. (14) and the number of current meter equations (n in Eq. (13)) would be significantly larger. In either case, the contribution of the weighted current meter error within the total error (Eq. (12)) would be the same.

The error in the shipboard ADCP data is the same as in the current meters except that it is not divided by the equivalent degrees of freedom since it is not seasonally averaged. In addition to having the same error as in the shipboard ADCP data, the drifter data have another significant source of error resulting from its lack of vertical resolution. The magnitude of this error is estimated using the shipboard ADCP data. This is done by computing the RMS of the differences between transports that use the entire shipboard ADCP velocity profile and only the velocity value closest to the surface. It should be noted that this error approximation does not include possible influences on the drifters associated with surface turbulence and wind waves. Therefore, drifter errors are probably higher than those estimated here.

The elements of the weighing matrix are determined by applying these expected errors along with the appropriate number of equations (n) in Table 1 to the formulation given in Eq. (13). These weights are only best estimates and contain inaccuracies. Numerous experiments were performed to test the sensitivity of the weights on the solution. Each weight was individually changed by plus and minus one order of magnitude to simulate a wide range of terms neglected in the estimation of the expected errors. This set of 24 solutions is not included within this paper in order to conserve space. The variation of each weight had little effect on the solution, therefore, implying that the solution is not overly sensitive to changes of the weights.

6. Results and discussion

6.1. General circulation

Best estimates for the seasonally averaged flow fields are computed for the LATEX and NEGOM shelves by assimilating the weighted current meter, shipboard ADCP, and drifter data (described in Section 3) with the weighted shallow water equations and boundary and smoothing constraints (described in Section 4). Plots of these seasonal solutions are displayed in Figs. 5 and 6. It should be noted that the solutions resulting from this assimilation are in terms of transport. However, to make these plots easier to visualize the solutions are divided by depth to put the flow fields in terms of barotropic velocity. It is also important to note that no SSH measurements are assimilated; therefore, the solutions for SSH are based solely on the geostrophic balance in the momentum equations. An arbitrary value (spatially constant) could be added to the SSH without changing the error to the momentum equations (Eqs. (2) and (3)). The spatial gradients of SSH, however, indicate how well geostrophy is satisfied.

To demonstrate the influence that the dynamics have on the inverse solution, Fig. 7 shows the solution resulting from assimilating the three weighted data sets for summer on the LATEX shelf with the weights of the momentum, continuity, and boundary constraint set to zero. This solution is therefore constrained to best fit just the observations and smoothing. Comparison of Figs. 5b and 7 reveals significant differences. In particular, without dynamics (Fig. 7), there are areas of large convergence and divergence in violation of continuity. Therefore, the assimilation of dynamics is required in order to produce an

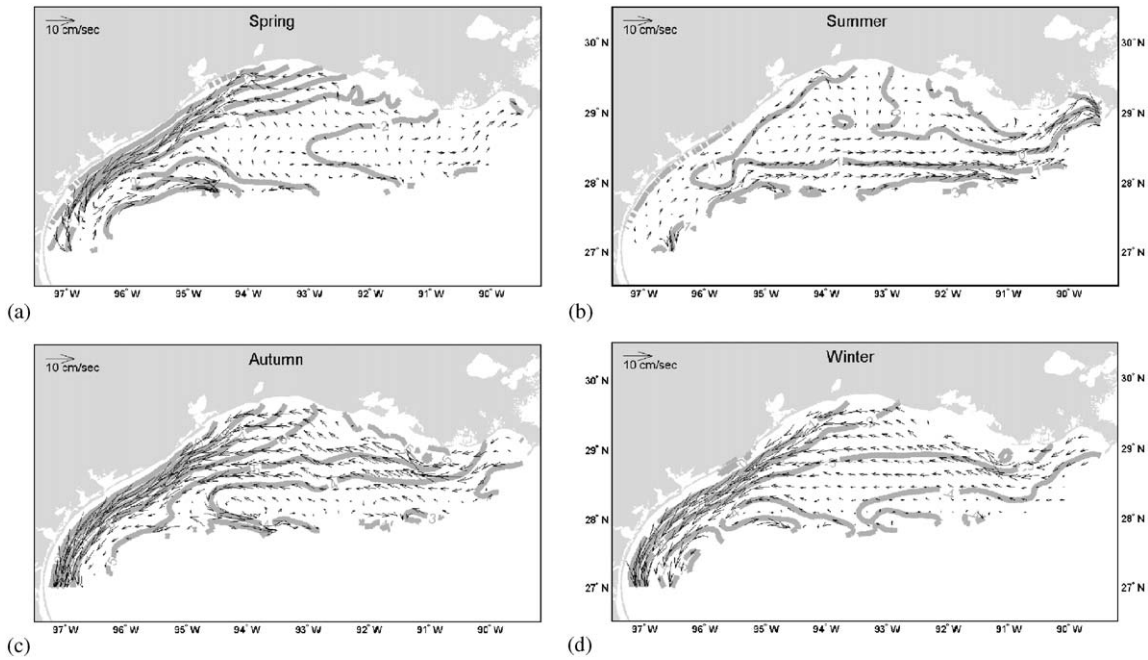

Fig. 5. Inverse solutions for the seasonal circulation for (a) spring, (b) summer, (c) autumn, and (d) winter are obtained by assimilating weighted dynamics with weighted current meter, shipboard ADCP, and drifter measurements on the LATEX shelf. The vectors represent seasonally and depth averaged velocities and the shaded contours are constant increments of SSH (cm). Note that since no SSH measurements are assimilated, SSH solutions are only a result of geostrophic balance in the momentum equations.

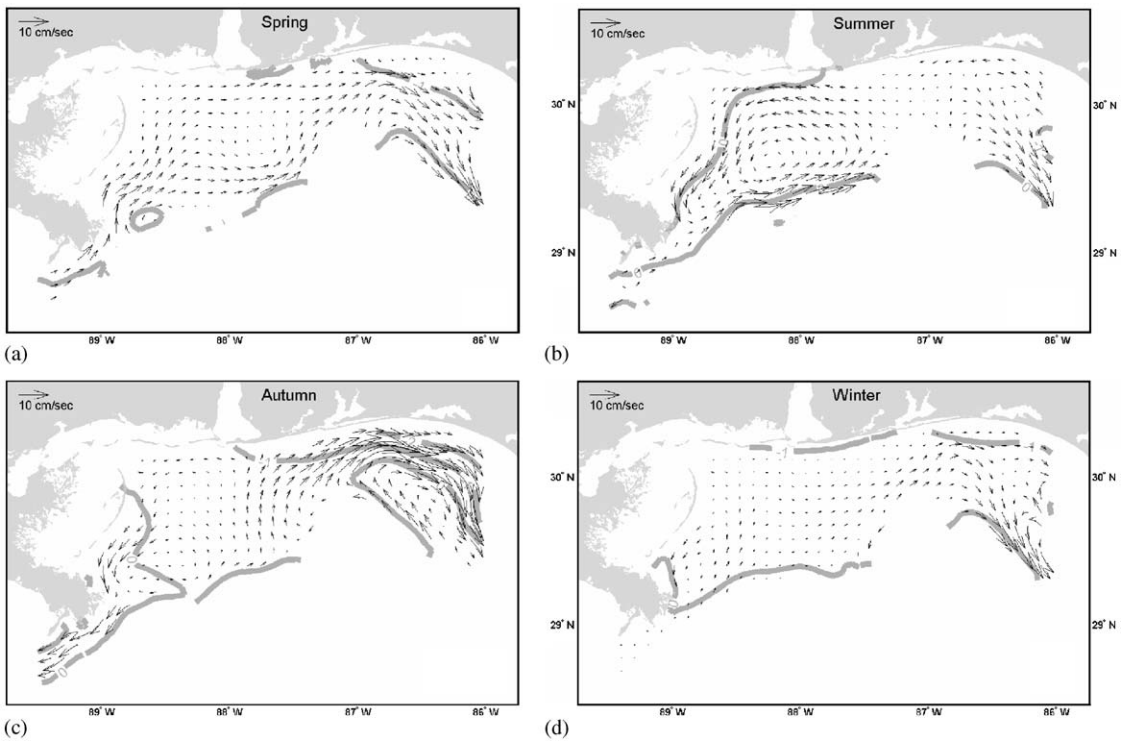

Fig. 6. This figure is the same as Fig. 5 except that it is for the NEGOM shelf.

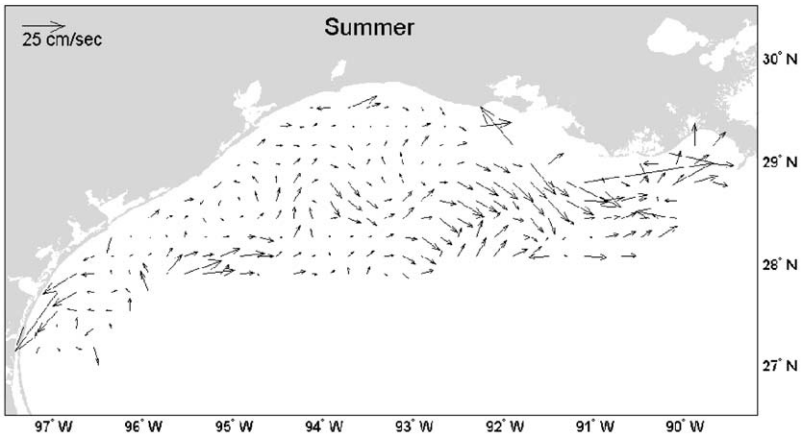

Fig. 7. Inverse solution without the assimilation of dynamics for summer on the LATEX shelf shows the influence that dynamics have on the solution. This figure is the same as Fig. 5b except that it includes only the assimilation of the weighted smoothing constraint with the three weighted data sets.

adequate, believable circulation field that is a best fit to three different types of data.

6.1.1. Louisiana–Texas shelf

The resulting flow fields on the LATEX shelf (Fig. 5) contain many of the same features that appear in previous estimates of the generalized circulation made by Cochrane and Kelly (1986), Li et al. (1996), and Cho et al. (1998). In the autumn and winter solutions, there is a strong westward/southwestward current along the entire coast of the solution domain. In the spring solution, there appears to be a northward flow at about 92°W; near the coast this flow splits with a strong westward along-shore current to the west and a slight eastward current to the east. In the summer solution, this northward flow shifts westward to about 93.5°W and the along-shore current west of this divergence is only slightly westward, whereas east of here the eastward current is much stronger. Cochrane and Kelly (1986) suggest that this splitting exists at 92.5°W and is due to bottom friction and wind stress divergence.

During autumn and winter northeasterly wind stresses dominate the LATEX shelf (Figs. 8c and d). Comparison of these wind stress fields with the strong westward and southwestward current along the Louisiana and Texas coast, respectively, in Figs. 5c and d indicates a correlation between the two. Cochrane and Kelly (1986) and Vastano et al. (1995) also believe that the along-shore components of these wind stresses are the primary cause of this coastal jet. During May and June the overall direction of the wind stress field shifts from northeasterly to southeasterly, which is mostly in the on-shore direction along the majority of the coastline. Cochrane and Kelly (1986) and Cho et al. (1998) suggest that this shift in wind direction causes the strong westward coastal jet to disappear, and by July the along-shore current flows slowly eastward. Then around mid-August there is an abrupt change in the prevailing wind direction back to northeasterly causing the westward coastal jet to return again. This description of the wind-driven coastal current agrees well with the solution in Fig. 5, except that in the summer solution this current is slightly westward west of 94°W, not eastward.

Another indication that the along-shore current is wind driven is apparent in the region close to the shore between about 92.5°W and 94.5°W in the non-summer solutions. The flow within this region does not follow the contours of SSH, which indicates geostrophy is not satisfied and that another mechanism (such as wind stress) is the leading contributor to momentum. Cochrane and Kelly (1986) and Oey (1995), however, suggest that the correlation between along-shelf winds and

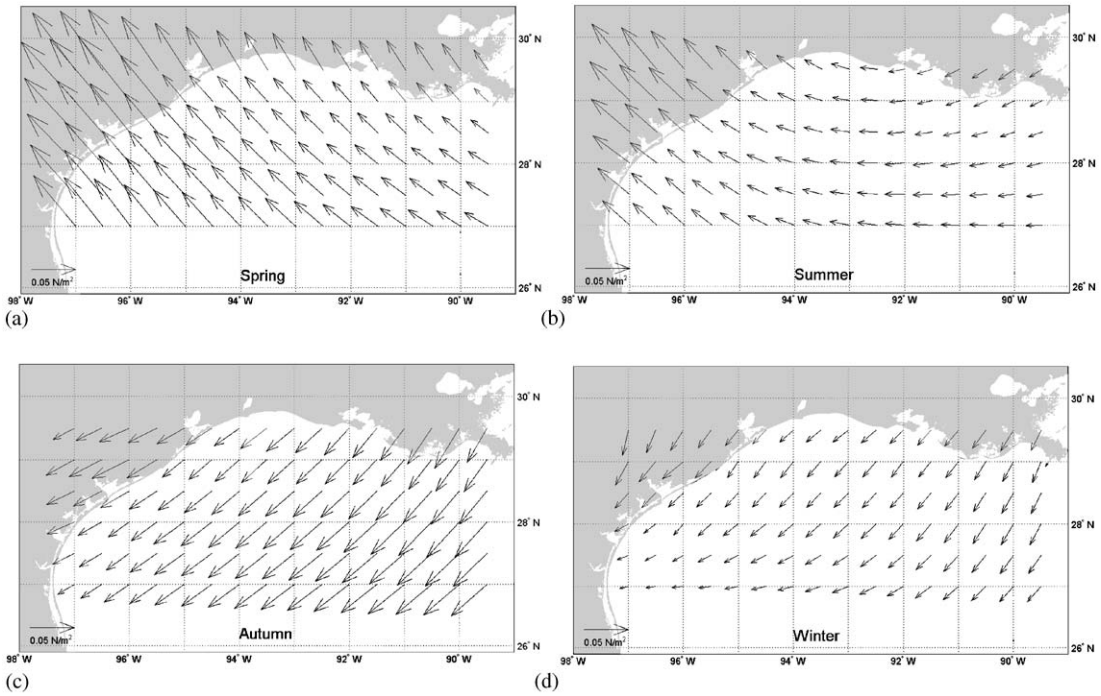

Fig. 8. Seasonally averaged wind stress fields are computed from 5 years of NOGAPS data and exhibit the progression of the wind field over the LATEX shelf.

along-shelf currents is weak on the eastern side of the LATEX shelf. Currents within this region can be influenced by open-ocean processes and intruding water and buoyancy processes caused by the Mississippi and Atchafalaya Rivers. In the summer solution (Fig. 5b), the northeastward flow on the eastern edge of the domain supports this hypothesis since the wind stress (Fig. 8b) at this location is in the opposite direction.

It is widely believed that the flow along the outer LATEX shelf and shelfbreak is predominantly eastward, is strongest on the west side of the shelf during spring, and has significant interannual variability (Oey, 1995; Jochens, 1997; Cho et al., 1998; Zavala-Hidalgo et al., 2003). Zavala-Hidalgo et al. (2003) suggest that the eastward flow along the LATEX shelfbreak is at its maximum during April and May as a result of the wind-driven northward current on the Tamaulipas–Veracruz shelf (just south of the Texas shelf). Throughout spring when this northward flow reaches the southern edge of the Texas shelf it encounters a southwestward coastal current and generates a convergence, which causes the northward flow to be diverted northeastward along the outer LATEX shelf. Oey (1995) suggests that this western convergence can also be created by the collision and stalling of westward propagating LCEs in the northwestern Gulf of Mexico. The maximum northeastward/eastward shelfbreak current resulting from this convergence is apparent in the spring solution (Fig. 5a). The summer solution also displays a predominant eastward flow along the shelfbreak.

In the autumn and winter solutions, however, there are only small portions along the shelfbreak where the flow is eastward, which causes the cyclonic gyre in these solutions to be much smaller than what is predicted by Cochrane and Kelly (1986) and Cho et al. (1998). In these solutions, the flow along the shelfbreak appears to be non-uniform due to cross-shelf transports at several locations, for example at 92.5°W in the autumn solution and 95.5°W in the winter solution.

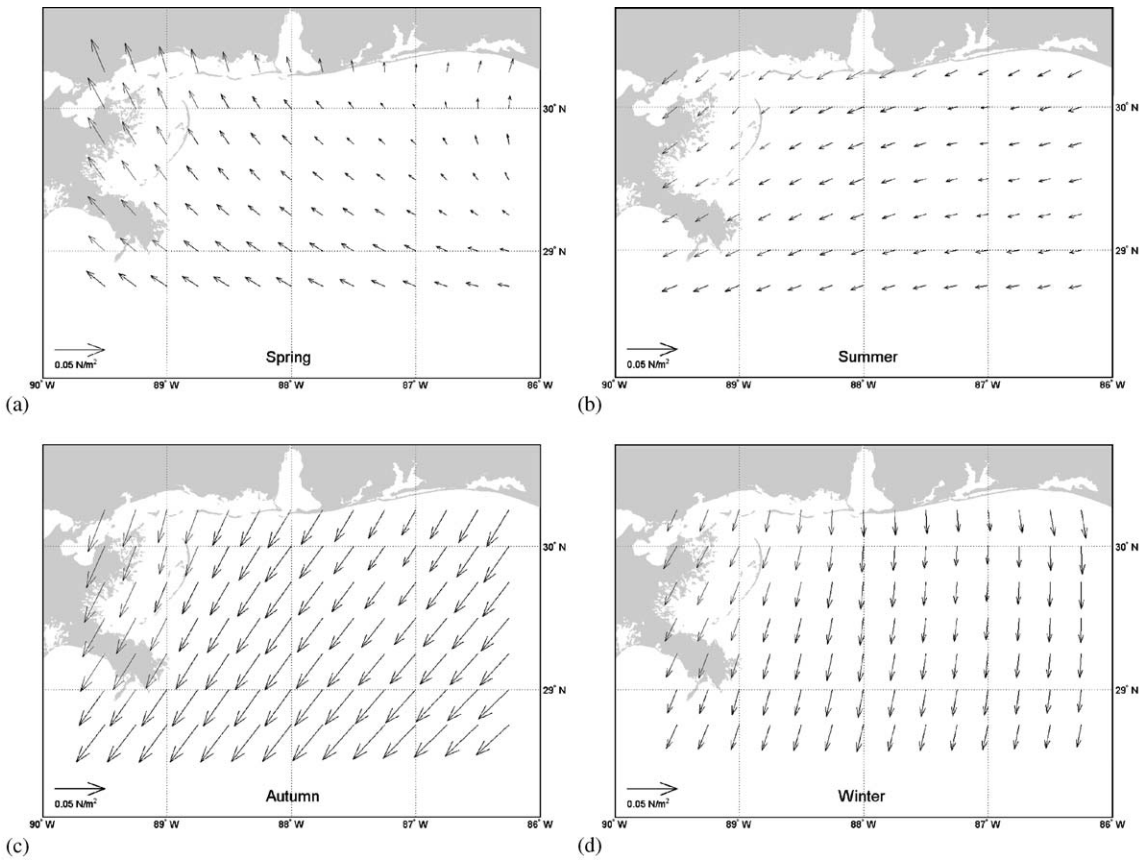

Fig. 9. This figure is the same as Fig. 8 except that it is for the NEGOM shelf.

Jochens (1997) demonstrates that the strongest eastward currents along the shelfbreak can be associated with nearby LCEs and westward currents can be associated with nearby cyclonic eddies. These cyclonic/anticyclonic eddy pairs also have the capacity to transport large quantities of water onto and off of the shelf (Jochens, 1997; Sahl et al., 1997).

6.1.2. *Northeast Gulf of Mexico shelf*

The resulting seasonal flow fields on the NEGOM shelf (Fig. 6) are mostly eastward, especially during spring, near the shelfbreak, and on the eastern portion of the shelf. Using the Princeton Ocean Model (POM), Weisberg and He (2003) also show that the flow along the shelf is predominantly eastward during spring of 1998. This dominant eastward flow is generally believed to be driven indirectly by the LC or LCEs.

In the summer, autumn, and winter solutions, there is a westward along-shore current on the western portion of the shelf. Comparison of these along-shore currents with the along-shore components of wind stress (Fig. 9) suggests that there is a strong correlation between the two. In the western portion of the summer solution, the easterly wind stress correlates well with the strong cyclonic coastal current. In the autumn solution, the slight westward coastal current is in response to the small easterly component of along-shore wind stress, and during winter both the coastal current and along-shore component of wind stress are virtually non-existent. Schroeder et al. (1987) also conclude that the coastal currents on the

NEGOM shelf are highly influenced by the easterly components of wind stress and typically flow westward, therefore producing cyclonic circulation (as is the case in Fig. 6b).

In the autumn solution, there is a slight northwestward current along the NEGOM shelfbreak between 86°W and 87°W. Using POM, Yang and Weisberg (1999) suggest that the wind-driven flow along the West Florida shelfbreak is predominantly northwestward during late summer and autumn. On the western side of the domain (near the tip of the Mississippi River Delta) the shelf is very narrow (only about 25 km) and the seasonal solutions reveal that the flow here is generally weak, except during autumn when there is a swift southwestward current (Fig. 6c). Wiseman and Dinnel (1988) also conclude that the shelf flow around the tip of the Mississippi Delta is typically very weak. The western boundary of the NEGOM domain is at the same location as the eastern boundary of the LATEX domain (89.5°W) and even though the solutions for the NEGOM and LATEX shelves are computed individually, the direction of the resulting currents at this common boundary compare favorably with one another. For example, during spring and summer the flow in both regions is eastward and during autumn the flow in both regions is westward.

Another important dynamic feature that exists on the NEGOM shelf is the cross-shelf intrusion of warm LC water on to the shelf in the DeSoto Canyon region (Huh et al., 1981). On occasion, large cyclonic and anticyclonic eddies associated with the LC can penetrate far enough north to cause cross-shelf flow, but in general shelf penetrations are a response to large wind events such as wind bursts, storms, and hurricanes (Hamilton et al., 2000). An example of this type of penetration results from an eastward current along the outer rim of the DeSoto Canyon following bathymetry contours. As this current flows around the relatively sharp bend of the canyon, there is a tendency for the flow to go up on to the shelf. During winter, northerly wind bursts can occur, which enhance the southward currents along the West Florida shelf. When this occurs the pressure gradient across the shelf increases, which induces strong cross-isobath flow at the head of the DeSoto Canyon (Hsueh and Golubev, 2002; Yuan, 2002). This cross-shelf intrusion is evident in the spring, summer, and winter solutions where the constant contours of SSH are perpendicular to the open boundary on the shelfbreak at 87°W.

6.2. Errors to dynamics and data

The computed solution is a best fit to the dynamics and observations. Thus it exactly satisfies neither. The extent to which the solution does not satisfy the dynamics or observations reveals information on either how accurate the dynamics are or how representative the measurements are. The absolute values of the errors in the equations of motion, constraints, and data are divided by their corresponding expected errors ($|\mathbf{A}\vec{\mathbf{x}} - \vec{\mathbf{b}}|/\langle er\rangle$) so that results are in terms of number of standard deviations (Std) of the expected errors. This makes it easy to identify areas in which errors are much larger than a priori estimates, therefore providing a check on each expected error. Typically, normalized error values should be between one and two. If a normalized error is much greater than three, then there are additional contributors to that error that were not originally considered. These errors are also useful for identifying where the solutions to the barotropic dynamics and the different measurement types agree or disagree with each other.

Spatial averages of the normalized errors in the LATEX and NEGOM shelves (Table 2) give an overall indication of how well the solutions agree with the proposed dynamics in each season. These mean errors show that continuity, boundary constraints, and SSH smoothing are satisfied well within expected values in both regions and during all seasons. Momentum, transport smoothing, and current meter data are satisfied well, but to a lesser degree. However, the mean normalized errors associated with the shipboard ADCP and drifter data are larger, though not well beyond expectations.

6.2.1. Distribution of error on Louisiana–Texas shelf

The distribution of the normalized errors associated with the momentum equations on the

Table 2
Spatially averaged errors in each set of dynamics and data for each season and region divided by the corresponding expected errors

	LATEX				NEGOM			
	Spring	Summer	Autumn	Winter	Spring	Summer	Autumn	Winter
Continuity	1×10^{-4}	3×10^{-4}	1×10^{-4}	8×10^{-5}	8×10^{-5}	9×10^{-5}	1×10^{-4}	7×10^{-5}
Momentum	0.17	0.22	0.21	0.18	0.17	0.20	0.22	0.14
Smoothing of U and V	0.13	0.14	0.16	0.11	0.16	0.16	0.24	0.13
Smoothing of SSH	0.04	0.04	0.06	0.04	0.05	0.05	0.08	0.04
Boundary constraint	0.02	0.02	0.02	0.02	0.02	0.02	0.02	0.01
Current meter	0.12	0.13	0.11	0.10	0.15	0.19	0.15	0.18
Shipboard ADCP	0.99	0.84	0.82	0.71	0.80	0.61	0.59	—
Drifter	0.38	0.33	0.40	0.44	0.73	0.92	1.04	0.78

Note: These spatially averaged normalized errors have units of number of standard deviations (Std) of the expected errors and are within expected values (errors are considered significant if they are greater than 3 Std).

LATEX shelf (Fig. 10) contains small patches of high error. There is a higher concentration of momentum error along the shelfbreak and a significant increase in error in the southwest corner of the shelf where errors approach 1 Std of the expected momentum error. The measurement errors have a similar distribution, with increased error near the shelfbreak, some of which surpassing 3 Std of their respective expected errors. The entrance of the western shelfbreak current (97°W, 27°N) exhibits the highest measurement errors. Oey (1995) suggests that there is a convergence in this region created by the collision and stalling of highly variable westward propagating LCEs. Jochens (1997) also points out that LCEs along with their accompanying cyclonic eddies passing nearby the shelfbreak have the capability to dominate the flow along the shelfbreak. Since the assimilated barotropic dynamics do not account for these baroclinic processes, a significant difference (error) between the flow predicted by measurements and dynamics can be expected.

6.2.2. *Distribution of error on Northeast Gulf of Mexico shelf*

The distribution of the normalized errors in the momentum equations and data on the NEGOM shelf (Fig. 11) are less than 1 Std of the expected value throughout most of the domain. However, there are numerous locations along the shelfbreak where the errors in both momentum and data well exceed this value. There are relatively large errors in momentum at localized regions such as: the head of the DeSoto Canyon (all seasons), the tip of the Mississippi Delta (spring and autumn), along the shelfbreak just west of the DeSoto Canyon (summer), and east of the DeSoto Canyon (summer, autumn, and winter). The errors in shipboard ADCP data are distributed evenly throughout the domain with a slight increase closer to the shelfbreak and the DeSoto Canyon. Whereas, there are very large errors in drifter data (up to 4 Std of its expected error) concentrated along the shelfbreak next to the DeSoto Canyon eastern wall. Errors of this magnitude indicate a failure of the drifter measurement ability to represent the seasonally averaged barotropic flow within this region.

It is apparent that a strong correlation exists between areas of large current meter data error and momentum error. For example, at the head of the DeSoto Canyon there is a large conflict between a current meter measurement and momentum, thus causing the measurement error to exceed 1 Std of its expected error and the momentum error to exceed well over 2 Std. This conflict is highest during winter, which happens to also be the same time of year when it is believed that maximum penetration across the canyon shelfbreak occurs (Hsueh and Golubev, 2002).

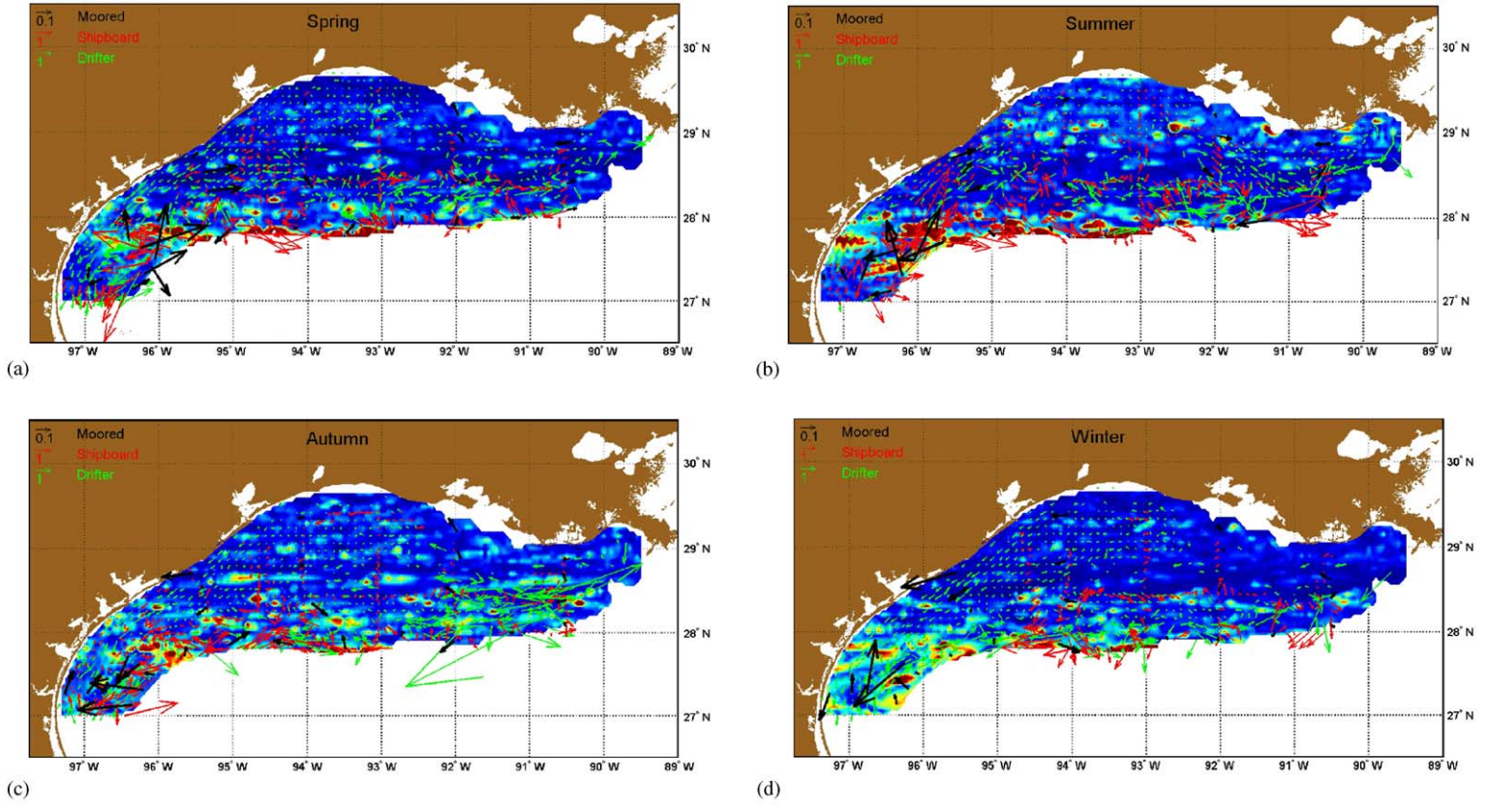

Fig. 10. Errors in the momentum equations (color), current meter measurements (black vectors), shipboard ADCP measurements (red vectors), and drifter measurements (green vectors) on the LATEX shelf show when and where the data and dynamics are in disagreement with a priori assumptions. These errors are in units of number of Std relative to their expected errors, and the momentum error ranges from 0 Std (blue) to $\geqslant 1$ Std (red). The errors in the data are spatially weighted to solution grid points and averaged for (a) spring, (b) summer, (c) autumn, and (d) winter. Note that since the overall current meter measurement error is significantly less than the overall shipboard ADCP and drifter errors (see Table 2), the scale for the current meter errors is an order of magnitude smaller than the scale for the shipboard and drifter errors.

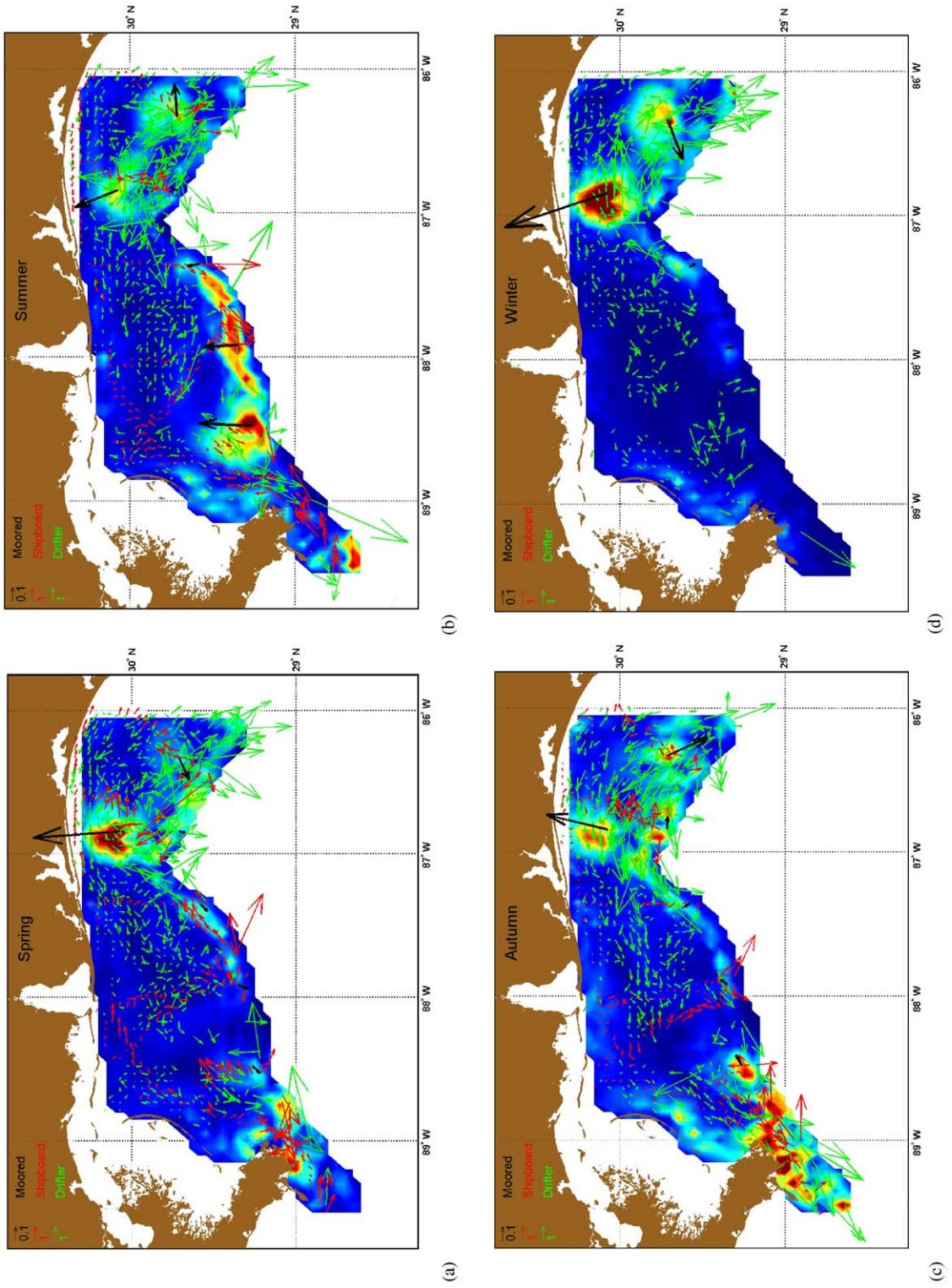

Fig. 11. This figure is the same as Fig. 10 except that it is for the NEGOM shelf.

The momentum equations are not equipped with the necessary dynamics to account for this intrusion.

6.2.3. Comparison between data types

Current meter data are able to represent the seasonally averaged vertically integrated flow better than the drifter and shipboard ADCP data, since they have longer temporal coverage at a particular point. This assertion is reflected in the estimation of the expected errors in Section 5.2. The expected errors in turn cause the current meter data to have more influence than the other two data sets in the estimation of the solutions within the vicinity of the current meter moorings. This explains why the overall error in the current meter data is considerably smaller than in the other two data sets. The drifter and shipboard ADCP data, however, do provide better spatial coverage (especially on the NEGOM shelf). Therefore, in regions far enough removed from the current meter moorings these two data types may have more influence on the solution.

Since it is clear that the solutions satisfy current meter data the best within their vicinity, it remains to be seen which of the two remaining data types more accurately estimates the overall seasonal flow fields on the LATEX and NEGOM shelves. The spatially averaged normalized errors in the shipboard ADCP and drifter data, listed in Table 2, reveal that the overall errors in shipboard ADCP data are higher on the LATEX shelf than on the NEGOM shelf, whereas the opposite is true with the drifter data. The seasonal average error including both data types is 0.78 on the NEGOM shelf and 0.61 on the LATEX shelf. Examination of the observations on both shelves (Figs. 3 and 4) reveals a considerable amount of conflict between the shipboard ADCP and drifter data sets, with conflict being more severe on the NEGOM shelf.

The best way to determine which of these two data types is more capable of estimating seasonal flow fields is to compute separate solutions using only the shipboard ADCP data and only the drifter data. The resulting seasonally averaged flow fields are displayed for autumn in Figs. 12 and 13 on the LATEX and NEGOM shelves, respectively. For this experiment the solution using all three data types (Figs. 5 and 6) is considered the optimal solution, which is heavily influenced by the current meter data. Comparison of Figs. 12 and 5c indicates that the shipboard ADCP data represent the flow on the LATEX shelf slightly better than the drifter data. The solution using drifter data matches Fig. 5c well, except that it is missing many small features along the shelfbreak. This discrepancy is most likely associated with the inability of the drifter data being able to resolve the baroclinic effects along the shelfbreak.

On the NEGOM shelf the results of this experiment suggest that the solution using only drifter data (Fig. 13b) matches the optimal solution (Fig. 6c) better than the solution using only shipboard ADCP data (Fig. 13b). There are considerable contradictions between the shipboard ADCP and optimal solutions. Fig. 13a does not reconstruct the northwestward current along the shelfbreak just east of the DeSoto Canyon and the south/southwestward current around the tip of the Mississippi Delta. This discrepancy is primarily a result of the shipboard ADCP and drifter data being collected during different years (Fig. 2), which in turn provides evidence that the NEGOM shelf has a considerable amount of interannual variability. This is confirmed by He and Weisberg (2003) whom reveal that 1998 was an anomalous year, and that during autumn the LC had an increased influence on the circulation along the Florida shelf causing a more substantial southeastward flow. Since the shipboard ADCP data includes this anomalous year and the drifter data does not, it is logical that Fig. 13a displays a more dominant southeastward flow on the eastern side of the NEGOM shelf.

Also, the optimal NEGOM solution may not represent the current meter data effectively since there are only six current meters; unlike the LATEX shelf which includes data from 29 current meters. In addition, there are more drifter measurements than shipboard ADCP measurements on the NEGOM shelf (Fig. 2), and the drifter data are dispersed over the shelf more uniformly (Fig. 4). Therefore, it is possible that even though the weight on the drifter data is the least of the three data types (the drifter data contains the highest error), there may be sufficient drifter observations

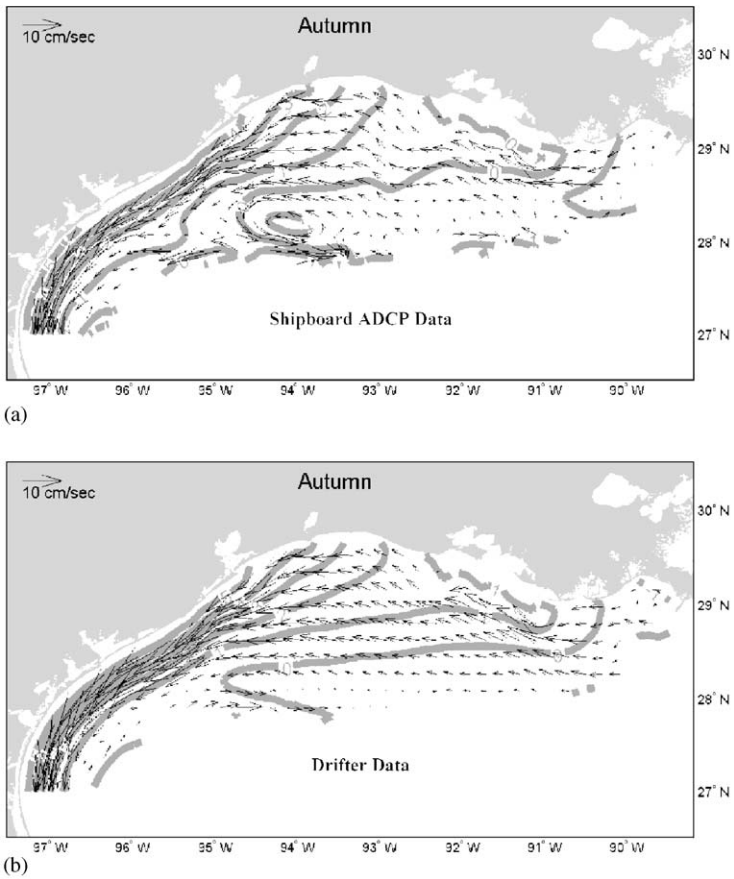

Fig. 12. This figure is similar to Fig. 5c except that instead of assimilating all three data types simultaneously, the weighted (a) shipboard ADCP and (b) drifter measurements are assimilated separately so that the influence that these two data types has on the general circulation can be compared.

on the shelf so that current meter and shipboard ADCP data are not as large of an influence on the solution, thus allowing the optimal solution to weigh more heavily on the drifter data. Within the LATEX region, a higher-quality data set (shipboard ADCP) seems to be more capable of representing the flow field. Whereas, in the NEGOM region, a lower-quality data set (drifter) is more influential. Thus, it is possible for quantity of observations to prevail over their quality.

7. Conclusions

Seasonally averaged circulation fields are calculated for the LATEX and NEGOM shelves by assimilating weighted current meter, shipboard ADCP, and drifter data with a system of barotropic dynamics, boundary constraints, and smoothing. The inclusion of dynamics is required in the assimilation process in order to produce a realistic circulation field that is a best fit to three different types of data (Fig. 7). The solutions for the LATEX shelf agree with prior studies, featuring a strong westward coastal current during the non-summer seasons and an overall eastward flow during summer (Fig. 5). The solutions for the NEGOM shelf exhibit an overall eastward flow, with a westward coastal current during summer and autumn (Fig. 6). Comparison of these solutions with the seasonal wind stress fields (Figs. 8 and 9) reveals that on the LATEX shelf the flow

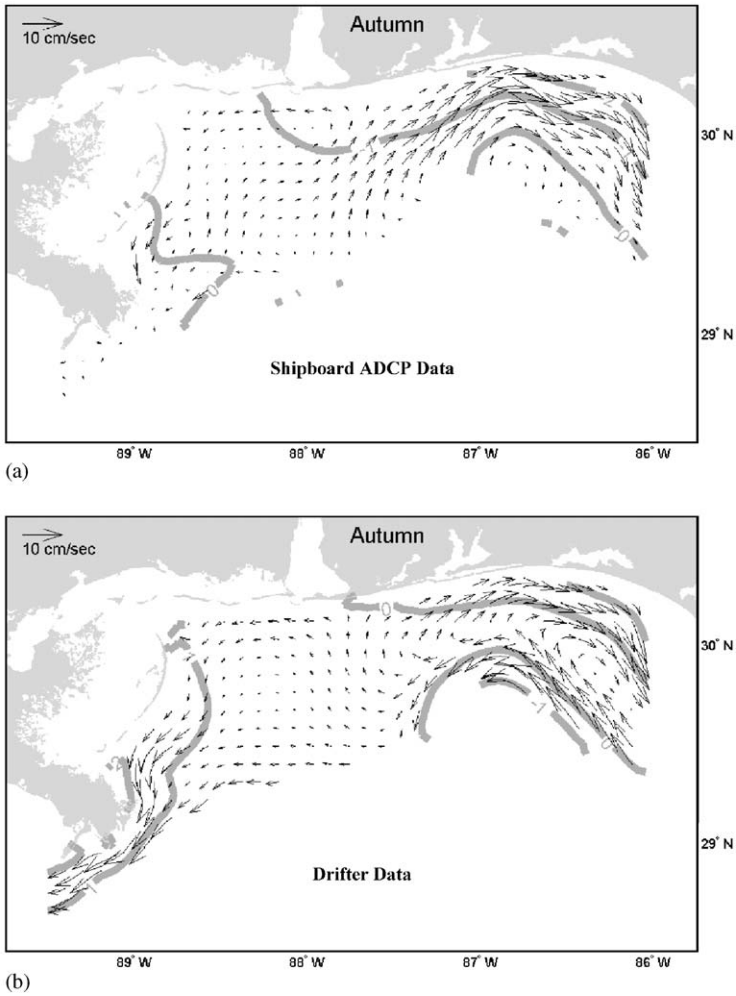

Fig. 13. This figure is the same as Fig. 12 except that it is for the NEGOM shelf.

near the coast west of 92.5°W is primarily wind driven. As for the flow on the NEGOM shelf, the flow is primarily wind-driven near the coast west of 87.5°W during summer, autumn, and winter.

Analysis of the spatially averaged errors in the dynamics and data relative to expected errors (Table 2) indicates that the solutions generally satisfy the system of equations within expected values. There are, however, relatively large errors in the momentum equations and data along the shelfbreaks of both regions with significant errors focused at the southwest corner of the LATEX shelf (Fig. 10) and at the head of the DeSoto Canyon on the NEGOM shelf (Fig. 11). At these locations there are processes occurring that cannot be described by the barotropic dynamics being used, therefore, causing the error in momentum and data to exceed their expected values. At the head of the DeSoto Canyon, the source of large error is believed to be a result of penetrating deep water across the shelfbreak. Whereas, the process that is causing the large error at the southwest corner of the LATEX shelf is believed to be converging flow. These results suggest that the simplified barotropic equations (Eqs. (1)–(3)), which do not resolve baroclinic effects such as

seasonal heating and cooling, shelfbreak boundary currents, and eddies, are not applicable along the shelfbreak.

The spatially averaged errors in the data indicate that the current meter data represent the seasonally averaged barotropic flow field most accurately, and that both the shipboard ADCP and drifter data do reasonably well. By assimilating the shipboard ADCP and drifter data sets individually for autumn (Figs. 12 and 13) and comparing with the solution using all three data sets, insight into the influence that each data set has on the flow in each region is gained. Results of this experiment imply that on the LATEX shelf the shipboard ADCP data represent the seasonal flow field slightly better than the drifter data. Whereas, on the NEGOM shelf results imply that the drifter data perform better. This conclusion however is skewed, since the shipboard ADCP and drifter data sets were collected on the NEGOM shelf during different years, and one of these years (1998) was anomalous in that the LC had a much larger influence in the circulation on the shelf.

Acknowledgements

This work was sponsored by the Office of Naval Research (program element PE0601153N) as part of the projects "Error Propagation in the Continental Shelf" and "Slope to Shelf Energetics and Exchange Dynamics". This work is a contribution of the Naval Research Laboratory, number NRL/JA/7320/04/0002. We would like to thank Thomas Berger and Peter Hamilton of Science Applications International Corporation for allowing the use of current meter and shipboard ADCP data as part of the project "DeSoto Canyon Eddy Intrusion Study", supported by grants from the Minerals Management Service. Additional thanks go to Texas A&M University and Minerals Management Service for the use of data from the "LATEX A Study" and the "Northeastern Gulf of Mexico Physical Oceanography Program: Chemical Oceanography and Hydrography Study". We also appreciate Dr. Peter Niiler and Dr. Carter Ohlmann supplying us with the SCULP drifter data sets. We are particular grateful for the many helpful suggestions provided by the reviewers of this manuscript.

References

Barrett, R., Berry, M., Chan, T.F., Demmel, J., Donato, J., Dongarra, J., Eijkhout, V., Pozo, R., Romine, C., Vorst, H., 1994. Templates for the Solution of Linear Systems: Building Blocks for Iterative Methods, second ed. SIAM, Philadelphia, PA, pp. 41–42.

Bender III, L.C., Kelly, F.J., 1996. LATEX shelf data report: acoustic Doppler current profiler. Texas A&M University, Department of Oceanography, Technical Report No. 96-3-T, College Station, TX (377pp).

Chen, C., Reid, R.O., Nowlin Jr., W.D., 1996. Near-inertial oscillations over the Texas–Louisiana shelf. Journal of Geophysical Research 101 (C2), 3509–3524.

Cho, K., Reid, R.O., Nowlin Jr., W.D., 1998. Objectively mapped stream function fields on the Texas–Louisiana shelf based on 32 months of moored current meter data. Journal of Geophysical Research 103 (C5), 10,377–10,390.

Cochrane, J.D., Kelly, F.J., 1986. Low-frequency circulation on the Texas–Louisiana Continental shelf. Journal of Geophysical Research 91 (C9), 10,645–10,659.

Csanady, G., 1984. Circulation in the Coastal Ocean. Reidel Publishing Co., Dordrecht, Holland, pp. 11–12.

DiMarco, S.F., Jochens, A.E., Howard, M.K., 1997. LATEX shelf data report: current meter moorings, April 1992 through December 1994. Texas A&M University, Department of Oceanography, Technical Report No. 97-01-T, College Station, TX (3701pp).

Fox, D.N., Barron, C.N., Carnes, M.R., Booda, M., Peggion, G., Gurley, J.V., 2002. The modular ocean data assimilation system. Oceanography 15 (1), 22–28.

Golubev, Y., Hsueh, Y., 2002. Low-frequency variability of surface currents on the Northeastern Gulf of Mexico (NEGOM) shelf. In: Hsueh, Y., Weisberg, R. (Eds.), Northeastern Gulf of Mexico Circulation Modeling Study: Draft Final Report. US Department of the Interior, Minerals Management Service, Gulf of Mexico OCS Region, New Orleans, LA, pp. 78–93.

Hamilton, P., Berger, T.J., Singer, J.J., Waddell, E., Churchill, J.H., Leben, R.R., Lee, T.N., Sturges, W., 2000. Desoto Canyon Eddy Intrusion Study, final report: technical report, vol. II. US Department of the Interior, Minerals Management Service, Gulf of Mexico OCS Region, New Orleans, LA (275pp).

He, R., Weisberg, R.H., 2002. West Florida shelf circulation and temperature budget for the 1999 spring transition. Continental Shelf Research 22 (5), 719–748.

He, R., Weisberg, R.H., 2003. West Florida shelf circulation and temperature budget for the 1998 fall transition. Continental Shelf Research 22 (5), 719–748.

Hogan, T.F., Rosmond, T.E., 1991. The description of the navy operational global atmospheric prediction system. Monthly Weather Review 119 (8), 1786–1815.

Hsueh, Y., Golubev, Y., 2002. A numerical model calculation of the flow in DeSoto Canyon in response to northerly wind bursts in winter. In: Hsueh, Y., Weisberg, R. (Eds.), Northeastern Gulf of Mexico Circulation Modeling Study: Draft Final Report. US Department of the Interior, Minerals Management Service, Gulf of Mexico OCS Region, New Orleans, LA, pp. 25–51.

Huh, O.K., Wiseman Jr., W.J., Rouse Jr., L.J., 1981. Intrusion of loop current waters onto the West Florida continental shelf. Journal of Geophysical Research 86 (C5), 4186–4192.

Jochens, A.E., 1997. Circulation over the Texas–Louisiana slope based on sea surface elevation and current velocity fields. Ph.D. Thesis, Texas A&M University, College Station, TX, unpublished.

Jochens, A.E., DiMarco, S.F., Nowlin Jr., W.D., Reid, R.O., Kennicutt II, M.C., 2002. Northeastern Gulf of Mexico chemical oceanography and hydrography study, synthesis report: technical report. US Department of the Interior, Minerals Management Service, Gulf of Mexico OCS Region, New Orleans, LA (587pp).

Le Dimet, F.X., Talagrand, O., 1986. Variational algorithms for analysis and assimilation of meteorological observations: theoretical aspects. Tellus 38A, 97–110.

Li, Y., Nowlin Jr., W.D., Reid, R.O., 1996. Spatial-scale analysis of hydrographic data over the Texas–Louisiana continental shelf. Journal of Geophysical Research 101 (C9), 20,595–20,605.

Li, Y., Nowlin Jr., W.D., Reid, R.O., 1997. Mean hydrographic fields and their interannual variability over the Texas–Louisiana continental shelf in spring, summer, and fall. Journal of Geophysical Research 102 (C1), 1027–1049.

Mesinger, F., Arakawa, A., 1976. Numerical Methods Used in Atmospheric Models, vol. 1. GARP Publication, Series No. 17, Word Meteorological Organization, Geneva.

Oey, L., 1995. Eddy- and wind-forced shelf circulation. Journal of Geophysical Research 100 (C5), 8621–8637.

Robinson, A.R., Lermusiaux, P.F.J., Sloan III., N.Q., 1998. Data assimilation. In: Brink, K.H., Robinson, A.R. (Eds.), The Sea, vol. 10. Wiley, New York, pp. 541–593.

Sahl, L.E., Wiesenburg, D.A., Merrell, W.J., 1997. Interactions of mesoscale features with Texas shelf and slope waters. Continental Shelf Research 17 (2), 117–136.

Schroeder, W.W., Dinnel, S.P., Wiseman Jr., W.J., Merrell Jr., W.J., 1987. Circulation patterns inferred from the movement of detached buoys in the eastern Gulf of Mexico. Continental Shelf Research 7 (8), 883–894.

Talagrand, O., 1997. Assimilation of observations, an introduction. Journal of the Meteorological Society of Japan 75, 191–209.

Vastano, A.C., Barron Jr., C.N., Shaar Jr., E.W., 1995. Satellite-observations of the Texas Current. Continental Shelf Research 15 (6), 729–754.

Wang, D., Oey, L., Ezer, T., Hamilton, P., 2003. Near-surface currents in DeSoto Canyon (1997–99): comparison of current meters, satellite observation, and model simulation. Journal of Physical Oceanography 33 (1), 313–326.

Weisberg, R.H., He, R., 2003. Local and deep-ocean forcing contributions to anomalous water properties on the West Florida Shelf. Journal of Geophysical Research 108 (C6), doi:10.1029/2002JC001407.

Wiseman, W.J., Dinnel, S.P., 1988. Shelf currents near the mouth of the Mississippi River. Journal of Physical Oceanography 18 (9), 1287–1291.

Yang, H., Weisberg, R.H., 1999. Response of the West Florida shelf circulation to climatological wind stress forcing. Journal of Geophysical Research 104 (C3), 5301–5320.

Yuan, D., 2002. A numerical study of barotropically forced intrusion in DeSoto Canyon. Journal of Geophysical Research 107 (C2), 2.1–2.15.

Zavala-Hidalgo, J., Morey, S.L., O'Brien, J.J., 2003. Seasonal circulation on the western shelf of the Gulf of Mexico using a high-resolution numerical model. Journal of Geophysical Research 108 (C12), 19.1–19.19.